

# Sub-wavelength imaging at infrared frequencies using an array of metallic nanorods

Mário G. Silveirinha

*Departamento de Engenharia Electrotécnica da Universidade de Coimbra,  
Instituto de Telecomunicações, Pólo II, 3030 Coimbra, Portugal*

Pavel A. Belov

*Department of Electronic Engineering, Queen Mary University of London,  
Mile End Road, London, E1 4NS, United Kingdom and  
Photonics and Optoinformatics Department, St. Petersburg State University of Information Technologies,  
Mechanics and Optics, Sablinskaya 14, 197101, St. Petersburg, Russia*

Constantin R. Simovski

*Photonics and Optoinformatics Department, St. Petersburg State University of Information Technologies,  
Mechanics and Optics, Sablinskaya 14, 197101, St. Petersburg, Russia  
(Dated: July 12, 2018)*

We demonstrate that an array of metallic nanorods enables sub-wavelength (near-field) imaging at infrared frequencies. Using an homogenization approach, it is theoretically proved that under certain conditions the incoming radiation can be transmitted by the array of nanorods over a significant distance with fairly low attenuation. The propagation mechanism does not involve a resonance of material parameters and thus the resolution is not strongly affected by material losses and has wide bandwidth. The sub-wavelength imaging with  $\lambda/10$  resolution by silver rods at 30 THz is demonstrated numerically using full-wave electromagnetic simulator.

PACS numbers: 78.20.Ci, 42.30.-d, 42.70.Qs

## I. INTRODUCTION

Recently, the problem of sub-diffraction imaging has attracted a lot of interest in the scientific community. In 2000, J. Pendry has shown that a left-handed material slab with negative index of refraction makes a perfect lens with unlimited resolution [1]. The key property that enables sub-diffraction imaging in Pendry's lens is the amplification of the evanescent spatial harmonics. This phenomenon is the result of the resonant excitation of surface waves supported by the interfaces of the left-handed material slab. However, it soon became evident that this imaging mechanism is strongly sensitive to losses and dispersion [2–4], besides the fact that practical implementations of left-handed materials are still a challenge. To overcome these obstacles, other mechanisms to achieve subwavelength imaging have been studied. Namely, some researchers explored the fact that photonic crystals may enable negative refraction close to the band-gap edges [5, 6]. Also, recently a planar magnetoinductive lens was proposed for near-field imaging at the microwave range [7]. This approach is based on the excitation of surface waves at two weakly coupled resonant interfaces to amplify the evanescent waves.

A sub-diffraction near-field imaging mechanism of a different kind has been proposed by other researchers [8–14]. This technique is based neither on negative refraction nor on the amplification of evanescent waves. The idea is to transport the evanescent waves through an engineered material (transmission device), rather than to amplify them. This canalization mechanism is possible if the incoming wave can couple most of its energy to

an electromagnetic mode of the material with phase velocity nearly independent of the transverse wave vector (i.e. the associated wave normal surface must be nearly flat). In our opinion, the best solution proposed thus far at microwave frequencies is the one reported in [14]. In this configuration the engineered material is formed by an array of perfectly conducting wires (wire medium) that guide the radiation "pixel by pixel" from the input plane to the output plane. As discussed in [14, 15], the wire medium lens is capable of transporting subwavelength images without significant distortion to nearly unlimited distances since the influence of losses is negligibly small. Moreover, the resolution of the transmission device is only limited by the spacing between the wires. The problem with the wire medium lens is that its design cannot be directly scaled to higher frequencies (infrared and optical domains) because metals lose their conducting properties, and consequently the electrostatics of the equivalent medium is significantly altered. The straightforward attempts to get sub-wavelength imaging at optical frequencies using rodged medium [16] encounter problems and limitations related to the effect of strong losses.

Recently a non-local permittivity model was proposed by the authors to describe the electrostatics of plasmonic rods [17]. This study enables the proper dimensioning and generalization of the transmission device proposed in [14] to higher frequencies. In [17] it was proved that a periodic array of rods with negative real part of permittivity (this is the case of all metals at infrared and optical frequencies) can be modeled using an effective permittivity tensor and that spatial dispersion effects need to be considered. Moreover, our studies showed

that despite the rods not being perfectly conducting, the equivalent medium still supports nearly dispersionless modes, and we speculated that such modes may be used to enable near-field subwavelength imaging at the infrared and optical domains.

In this work, we will extend the theory proposed in [17] and demonstrate that in fact silver nanorods enable subdiffraction imaging up to terahertz (THz) and infrared (IR) region of the electromagnetic spectrum. In recent years, THz and IR radiation has attracted special attention, because it offers scientific and technological opportunities in many fields, such as in telecommunications, in computer technology, in spectroscopy, and in sensing [18]. Near-field imaging at THz and IR frequencies may be very important for diverse applications, such as the near-field microscopy of surfaces, recording information with increased storage capacity, or detecting and measuring the mass and volume fractions of bio cells (e.g. cells of blood), many organic molecules, radioactive atoms, microbes, viruses and explosive matters.

The paper is organized as follows. In section II we briefly review the electrodynamics of the plasmonic rod medium, and the possibility of canalizing waves through a rod medium slab. In section III we explain how to properly design the electromagnetic crystal in order to ensure that the phase velocity of waves is independent of the transverse wave vector. Next, in section IV we introduce an homogenization technique that enables the accurate analytical characterization of the transmission properties of a rod medium slab. In section V it is explained how to tune to thickness of the transmission device in order that it is operated in the canalization regime. In section VI we present full wave simulations that illustrate the potentials of the proposed configuration, and demonstrate subwavelength imaging at 30THz. Finally, in section VII the conclusions are presented.

In this work the fields are assumed monochromatic with time dependence  $e^{+j\omega t}$ .

## II. CANALIZATION OF WAVES THROUGH THE ROD MEDIUM

In order to enable the proper study and design of waveguiding structures based on plasmonic rods, next we review the homogenization theory introduced in [17]. Let us consider a periodic array of plasmonic rods oriented along the  $z$ -direction, as depicted Fig. 1 The rods are infinitely long, with radius  $R$ , and the spacing between the rods (lattice constant) is  $a$ . The rods are embedded in a dielectric host with permittivity  $\varepsilon_h$ . The permittivity of the rods is  $\varepsilon_m$ .

In [17] it was proved that for long wavelengths the fields in the periodic structure can be characterized using a nonlocal permittivity dyadic:

$$\overline{\overline{\varepsilon}}(\omega, k_z) = \varepsilon_h [\varepsilon_t(\mathbf{xx} + \mathbf{yy}) + \varepsilon_{zz}(\omega, k_z)\mathbf{zz}], \quad (1)$$

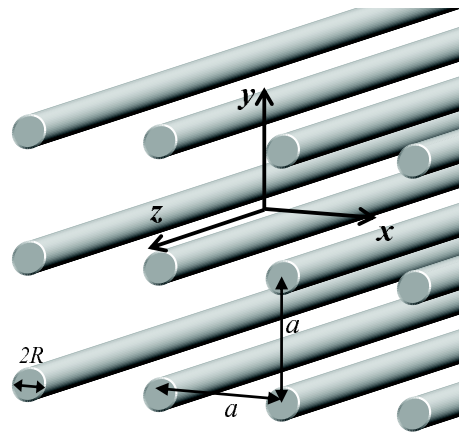


FIG. 1: Periodic array of long thin plasmonic rods arranged in a square lattice.

$$\varepsilon_t = 1 + \frac{2}{\frac{1}{f_V} \frac{\varepsilon_m + \varepsilon_h}{\varepsilon_m - \varepsilon_h} - 1}, \quad (2)$$

$$\varepsilon_{zz}(\omega, k_z) = 1 + \frac{1}{\frac{\varepsilon_h}{(\varepsilon_m - \varepsilon_h)f_V} - \frac{\beta^2 - k_z^2}{\beta_p^2}}, \quad (3)$$

where  $f_V = \pi R^2/a^2$  is the volume fraction of the rods,  $k_z$  is the  $z$ -component of the wave vector,  $\beta = \omega\sqrt{\varepsilon_h\mu_0}$  is the wave number in the host medium, and  $\beta_p$  is the plasma wave number for perfectly conducting rods given by [17, 19]:

$$(\beta_p a)^2 \approx \frac{2\pi}{\ln\left(\frac{a}{2\pi R}\right) + 0.5275}. \quad (4)$$

As discussed in [17], provided the permittivity of the rods is such that  $|\varepsilon_m| \gg \varepsilon_h$  and the rods are thin, then  $\varepsilon_t \approx 1$ . That is the case here since the plasma frequency of metals is well above the far infrared band.

It is well known [20–23], that the permittivity of metals at infrared and optical frequencies can be accurately described by the Drude model:

$$\varepsilon_m(\omega) = \varepsilon_0 \left( \varepsilon_\infty - \frac{\omega_m^2}{\omega^2 - j\omega\Gamma} \right), \quad (5)$$

where  $\omega_m$  and  $\Gamma$  are the plasma and damping frequencies of the material, respectively. To give further insights into the permittivity model, let us temporarily consider that losses can be neglected in the frequency window of interest, and that  $\omega \ll \omega_m$ . In these circumstances, substitution of (5) into (3) gives

$$\varepsilon_{zz} \approx 1 - \frac{\beta_p^2}{\left(1 + \frac{\beta_p^2}{f_V \beta_m^2}\right) \beta^2 - k_z^2}, \quad (6)$$

where we put  $\beta_m = \omega_m\sqrt{\varepsilon_0\mu_0}$ . By direct inspection of (6), it is clear that wave propagation in the  $xy$ -plane

(i.e.  $k_z = 0$ ) with electric field polarized along the rods is only possible when  $\beta > \beta_{\text{cut-off}}$ , where:

$$\beta_{\text{cut-off}}^2 = \frac{1}{\frac{1}{\beta_p^2} + \frac{1}{f_V \beta_m^2}}. \quad (7)$$

Hence, the cut-off frequency of the structure is determined by both the plasmonic properties of the metal and by the plasmonic properties intrinsic to the geometry of the structure.

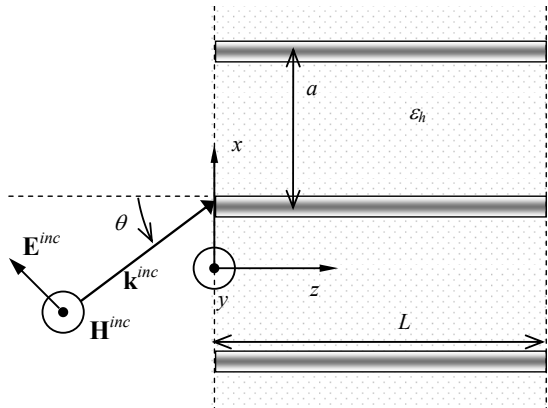


FIG. 2: A plane wave illuminates a slab of the rod medium (sideview). The thickness of the slab is  $L$  and the rods are normal to the interface. The structure is periodic along the  $x$  and  $y$  directions.

The idea to achieve sub-diffraction imaging is to guide the electromagnetic fields through an array of metallic rods normal to the front and back interfaces, as illustrated Fig. 2. The canalization phenomenon occurs when the phase velocity of an electromagnetic mode is nearly independent of the transverse wave vector. Next, we study in which circumstances can this happen.

We consider that the thickness of the slab is  $L$ , and that for  $z < 0$  and  $z > L$  the medium is air. A plane wave with transverse wave vector  $\mathbf{k}_{\parallel} = (k_x, k_y, 0)$  illuminates the slab (Fig. 2 depicts the case  $k_y = 0$ , which is assumed throughout this section without loss of generality). The incident magnetic field is parallel to the interface (the wave is transverse magnetic with respect to the  $z$ -direction). As is well-known, the transverse component of the wave vector is preserved at the boundary. The incident wave excites two TM-polarized electromagnetic modes in the rod medium with propagation constants  $k_z^{(1)}$  and  $k_z^{(2)}$ , respectively:

$$\left(k_z^{(1,2)}\right)^2 = \frac{1}{2} \left\{ \varepsilon_t \left( \beta^2 - k_{\parallel}^2 \right) + \left( \beta^2 + \beta_c^2 - \beta_p^2 \right) \right. \\ \left. \pm \sqrt{\left[ \varepsilon_t \left( \beta^2 - k_{\parallel}^2 \right) - \left( \beta^2 + \beta_c^2 - \beta_p^2 \right) \right]^2 + 4 \varepsilon_t k_{\parallel}^2 \beta_p^2} \right\}, \quad (8)$$

where

$$\beta_c^2 = -\frac{\varepsilon_h \beta_p^2}{(\varepsilon_m - \varepsilon_h) f_V}. \quad (9)$$

Note that (8) was obtained by solving the dispersion equation for the rod medium in the same manner as in [17]; it simplifies to the result (23) presented in [17] when  $\varepsilon_t = 1$ .

When the permittivity of the rods follows the Drude model (5) and the losses are negligible,  $\beta_c$  is to a first approximation a positive real number, (with the same unities as  $\beta$ ), that increases linearly with frequency:

$$\beta_c \approx \frac{\beta_p}{\sqrt{f_V} \beta_m} \beta. \quad (10)$$

As referred before, the canalization of waves through the engineered material is possible if either  $k_z^{(1)}$  or  $k_z^{(2)}$  are nearly independent of the transverse wave vector  $\mathbf{k}_{\parallel}$  [12]. In that case all the spatial harmonics suffer the same phase-shift when they propagate through the rod medium slab (see Fig. 2), provided the length  $L$  is also properly chosen [12]. In [17], two different opportunities to get flat isofrequency contours were identified. It was shown that if either  $\beta_c \ll \beta_p$  or  $\beta_c \gg \beta_p$ , or equivalently, using (10) and supposing that the permittivity of the host is comparable to that of free-space, if either  $\omega \ll \omega_m \sqrt{f_V}$  or  $\omega \gg \omega_m \sqrt{f_V}$ , the propagation constant of one of the modes, given by (8), becomes nearly independent of  $\mathbf{k}_{\parallel}$ . The two possibilities are summarized below:

1.  $\omega \ll \omega_m \sqrt{f_V}$ . In this case the nearly dispersionless mode is quasi-TEM, and has characteristics similar to the transmission line modes of the wire medium [19]. The radiation is not able to effectively penetrate into the rods, and so most of the energy propagates in the host medium. The isofrequency contour of the pertinent mode gets flatter as  $\frac{\beta_p}{\sqrt{f_V} \beta_m}$  decreases. Note that recently [24, 25], it was experimentally proved that a related propagation mechanism enables waveguiding of electromagnetic energy at THz frequencies.
2.  $\omega \gg \omega_m \sqrt{f_V}$ . In this case, the propagation mechanism is based on the surface plasmon-polariton supported by each rod. The energy of this surface wave is tightly bounded to the plasmonic material, and consequently there is no interaction or coupling between the rods (this is why the mode becomes dispersionless). When  $\frac{\beta_p}{\sqrt{f_V} \beta_m}$  increases the field confinement also increases, and the isofrequency contours become more flat.

Which of these possibilities is more interesting to achieve near-field sub-diffraction imaging? The answer is directly related to the effect of losses. Indeed, in the first case, since the field energy is mostly concentrated in the host medium [25], it is expected that the rod material losses have a mild effect on the propagation properties. Quite differently, in the second case, the surface plasmon-polariton has a field distribution tightly bounded to the metallic rods [26], and so the effect of losses may be dramatic, and ultimately destroy the possibility of imaging

as it was demonstrated in [16]. Hence, in this work we will explore the first regime, for which, as referred above, the rods support a quasi-TEM mode.

Firstly, we will study the influence of  $\omega_m$  on the properties of the modes. We consider propagation along the rod axes,  $k_{\parallel} = 0$ , and use the fact that  $\varepsilon_t \approx 1$ . Then (8) yields,

$$\begin{aligned} k_0^{(1)} &\equiv k_z^{(1)} \Big|_{k_{\parallel}=0} = \beta \sqrt{\varepsilon_t} \approx \beta \\ k_0^{(2)} &\equiv k_z^{(2)} \Big|_{k_{\parallel}=0} \approx -j \sqrt{\beta_p^2 - \beta_c^2 - \beta^2} \end{aligned} \quad (11)$$

Thus, the first mode has no cut-off and propagates nearly with the speed of light in the dielectric host, while the second mode can only propagate above the cut-off frequency given by (7). On the other hand, letting  $k_{\parallel} \rightarrow \infty$ , we find that:

$$\begin{aligned} k_{\infty}^{(1)} &\equiv k_z^{(1)} \Big|_{k_{\parallel}=\infty} \approx \sqrt{\beta^2 + \beta_c^2} \\ k_{\infty}^{(2)} &\equiv k_z^{(2)} \Big|_{k_{\parallel}=\infty} = -j\infty \end{aligned} \quad (12)$$

Hence, for off-axis propagation, the attenuation of the second mode increases. Quite differently, the first mode is never cut-off and may be nearly dispersionless. Indeed, using (10) we can write that,

$$k_{\infty}^{(1)} \approx \beta \sqrt{1 + \frac{\beta_p^2}{f_V \beta_m^2}} \quad (13)$$

and so it is evident that when  $\frac{\beta_p}{\sqrt{f_V} \beta_m}$  is small  $k_0^{(1)}$  and  $k_{\infty}^{(1)}$  are nearly identical, and the isofrequency contour is almost flat. In this case, the mode becomes quasi-TEM. Notice that if the rods are perfectly conducting then  $k_z^{(1)} = \beta$  for any  $k_{\parallel}$  and the mode is completely dispersionless and exactly TEM (transmission line mode of the wire medium [19]). In general, to obtain good imaging at a given design frequency, the rods material shall be chosen such that the plasma frequency  $\omega_m$  is as high as possible. To give an idea of the possibilities, we refer that the plasma and damping frequencies of the following metals are: aluminium (Al) 3570/19.4 THz, copper (Cu) 1914/8.34 THz, gold (Au) 2175/6.5, and silver (Ag) 2175/4.35 THz [20, 21, 23].

### III. DIMENSIONING OF THE RODS

In order to properly dimension the engineered material, it is also of obvious importance to assess the effect of the rods spacing  $a$ , and radius  $R$ , on the propagation characteristics. In order to study the isofrequency contours of the quasi-TEM mode, we use (4), (11) and (13) to obtain:

$$\frac{k_{\infty}^{(1)}}{k_0^{(1)}} \approx \sqrt{1 + \frac{1}{(\beta_m R)^2} \frac{2}{\ln\left(\frac{a}{2\pi R}\right) + 0.5275}} \quad (14)$$

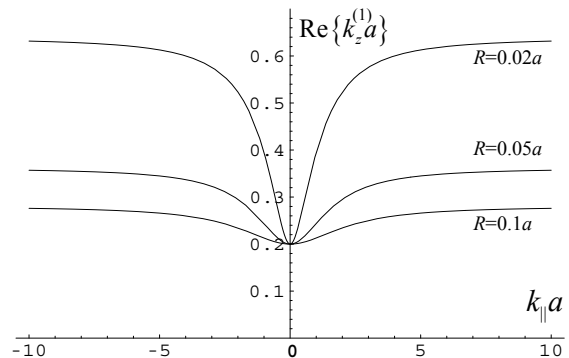


FIG. 3: Dispersion contours for the quasi-TEM mode at 30 THz for silver rods with  $a = 215\text{nm}$  and various values of  $R$ .

This result shows that  $a$  has little influence on the dispersion of the quasi-TEM mode, while the radius  $R$  is the main factor that determines how close to unity the ratio  $k_{\infty}^{(1)}/k_0^{(1)}$  is. Indeed, if the rods are too thin so that  $\beta_m R \ll 1$ , the isofrequency contours are not anymore flat. This is illustrated in Fig. 3, where we plot the isofrequency contours for a medium of silver rods at 30 THz ( $\varepsilon_{Ag} \approx -5143 - 746j$ ), for different values of  $R$ . The host medium is assumed to be Halcogenide glass,  $\varepsilon_h/\varepsilon_0 = 2.2$ , and the lattice constant is  $a = 215\text{nm}$  (i.e.  $\beta a = 0.2$ ). In Fig. 3 it is seen that the contours become hyperbolic when the radius of the rods is very small. Notice that the skin-depth in the rod material is given by  $\delta \approx 1/\beta_m$ . Hence, the condition to get flat contours is equivalent to  $\delta \ll R$ , i.e. the metal skin-depth must be much smaller than the radius of the wire.

For the imaging application it is essential that not only the phase velocity of one of the modes is independent of  $k_{\parallel}$ , but also that the other mode is severely attenuated so that it cannot be excited and interfere with the propagating mode. Thus, it is desirable that  $\text{Im}\{-k_z^{(2)}\}$  is as large as possible. From (11) one can verify that  $\text{Im}\{-k_0^{(2)} a\}$  increases either when the lattice constant  $a$  decreases, or when the ratio  $R/a$  increases. As before, this means that very thin rods may adversely affect the propagation characteristics of the mode with propagation constant  $k_z^{(2)}$ . This is illustrated in Fig. 4, where we plot the normalized attenuation constant as function of  $k_{\parallel}$  for different values of  $R$ . The rest of the parameters are as in the previous example. Nevertheless, the crucial factor that determines how severely the non-propagating mode is attenuated, is not the radius  $R$  but the lattice constant  $a$ . In fact, it can be verified that  $k_z^{(2)}$  is roughly proportional to  $1/a$ . This has a very important implication. Indeed, the total attenuation (in dBs) for a fixed distance  $L$  (see Fig. 2) will be proportional to  $L/a$ . Hence, in general, the smaller the lattice constant is the more attenuated the mode is. Assuming that  $L$  is comparable to the wavelength in the host material, this implies that

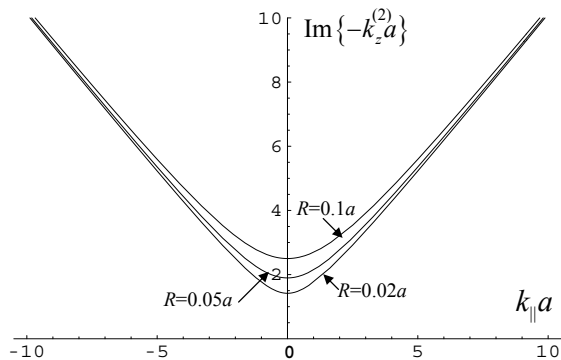


FIG. 4: Normalized attenuation constant (non-propagating mode) at 30 THz for Silver rods with  $a = 215nm$  and different values of  $R$ .

$a$  must be chosen such that  $\beta a \ll 1$ .

Let us summarize our findings. The spacing between the wires  $a$  must be chosen such that  $\beta a \ll 1$ . This ensures that the mode in cut-off is strongly attenuated and does not interfere with the quasi-TEM mode. On the other hand, to guarantee that the phase velocity of the quasi-TEM mode is nearly independent of the transverse wave vector, we need to choose the radius of the rods,  $R$ , at least as large as the metal skin-depth  $\delta$ . Since  $2R < a$ , it is clear that the two objectives may be contradictory, and that a trade-off may be necessary.

Moreover, as discussed next, the ratio  $R/a$  must also be kept relatively small, i.e. large values for  $R/a$ , let us say  $R/a > 0.1$ , cannot be admitted (also we remind the reader that the permittivity model (3) is only valid for diluted systems). The reason for this restriction is related to the transverse impedance. Indeed, for thick rods the cross-sectional area occupied by the metal is large, and this tends to make the transverse impedance small. This effect is obviously undesired because it deteriorates the matching with the exterior, and ultimately the bandwidth of the imaging system.

In practice, when the performance of the engineered material is mainly limited by the plasmonic properties of the rods, the best solution is to fix  $R$  slightly larger than the metal skin-depth, and choose  $a$  such that  $R/a < 0.1$ . If this solution yields a relatively small value for  $\beta a$ , then imaging with good quality can still be achieved. Notice that for very good conductors, the skin-depth can be neglected, and so it is always possible to design the engineered material in such a way that it has excellent imaging properties [14, 15].

#### IV. TRANSMISSION COEFFICIENT

So far, the possibility of near-field imaging was discussed mostly in a qualitative way. A more quantitative and detailed study requires the calculation of the trans-

mission coefficient for the configuration shown in Fig. 2. As referred in [17], even though the permittivity model of the medium is known, the calculation of the transmission coefficient is not trivial. The problem is that a TM-polarized incident wave (i.e. with magnetic field parallel to the interface) will excite two distinct TM-modes inside the rod medium slab, as discussed in section II. This phenomenon is a manifestation of strong spatial dispersion [27], and has an important consequence: the continuity of the tangential electric and magnetic fields at the interface is insufficient to calculate the scattering parameters; note that for TM-incidence, the TE-mode, with electric field parallel to the interface, cannot be excited [17]. Thus, because of the additional TM-mode in the artificial material slab, the system has one degree of freedom. To remove this degree of freedom, an additional boundary condition (ABC), besides the continuity of the tangential electromagnetic fields, is necessary.

In [28] an ABC was formulated and successfully validated for the case of perfectly conducting rods. The ABC establishes that,

$$\varepsilon_h E_n \text{ is continuous} \quad (15)$$

at the interfaces, where  $E_n$  is the normal component of the (average) electric field (i.e.  $E_z$  in Fig.2) and  $\varepsilon_h$  is the permittivity of the host medium (which in general can be different in the rod medium slab and in the regions  $z < 0$  and  $z > L$ ). Can such ABC be used for the case of non perfectly conducting rods?

In what follows, we demonstrate that the answer is positive. We will show that the physical arguments used in [28] can be adapted to the case of plasmonic rods. Let us consider the structure depicted in Fig.2. The polarization current (relative to the host medium) inside the plasmonic rods is given by  $\mathbf{J}_d = j\omega(\varepsilon_m - \varepsilon_h)\mathbf{E}$ , where  $\varepsilon_m$  is the permittivity of the rods (for perfectly conducting rods, the polarization current flows uniquely on the surface of the rods). At the interfaces the path along which the current flows (i.e. the rods) has an abrupt discontinuity. Indeed, provided  $|\varepsilon_m/\varepsilon_0| \gg 1$  the polarization current lines are not able to penetrate into the regions  $z < 0$  and  $z > L$ , and thus the  $z$ -component of the polarization current must be nearly null at the interfaces. Moreover, as in [28], it can be proved that following relation holds:

$$\left(\frac{\partial}{\partial z}\hat{\mathbf{u}}_z - j\mathbf{k}_{||}\right) \times \mathbf{H}_{\text{av}} = j\omega\varepsilon_h(z)\mathbf{E}_{\text{av}} + \frac{1}{a^2} \int_D \mathbf{J}_d e^{j\mathbf{k}_{||} \cdot \mathbf{r}} dx dy \quad (16)$$

where  $\mathbf{E}_{\text{av}}(z; \mathbf{k}_{||})$  and  $\mathbf{H}_{\text{av}}(z; \mathbf{k}_{||})$  represent the fields averaged over a  $z = \text{const.}$  cross-section of the unit cell, and  $D$  is the cross section of the rod. But since the tangential average electromagnetic fields are continuous at the interfaces and, as discussed above, the  $z$ -component of the polarization current vanishes at the interfaces, the above relation implies that the ABC (15) holds, as we wanted to establish (for more details see [28]).

Using (15), we can now easily study the transmission properties of the rod medium slab. Referring to Fig. 2, and assuming that the incident magnetic field is along the  $y$ -direction and has amplitude  $H_0$ , we can write that:

$$H_y = H_0 e^{-jk_x x} \begin{cases} e^{-jk_z^{(a)} z} + \rho e^{jk_z^{(a)} z}, & z < 0 \\ A_1 e^{-jk_z^{(1)} z} + A_2 e^{jk_z^{(1)} z} \\ + B_1 e^{-jk_z^{(2)} z} + B_2 e^{jk_z^{(2)} z}, & 0 < z < L \\ T e^{-jk_z^{(a)}(z-L)}, & z > L \end{cases} \quad (17)$$

where  $\rho$  is the reflection coefficient,  $T$  is the transmission coefficient,  $k_z^{(a)} = -j\sqrt{k_{\parallel}^2 - \varepsilon_0\mu_0\omega^2}$  is the longitudinal component of the wave vector in the free space regions, and  $A_1$ ,  $A_2$ ,  $B_1$ , and  $B_2$  are the unknown amplitudes of the TM-modes in the slab. We remember that for the case illustrated in Fig. 2, the transverse wave vector is  $k_{\parallel} = (k_x, 0, 0)$ . For a propagating incident wave, the

angle of incidence is such that  $\sin\theta = k_{\parallel}/\beta_0$  where  $\beta_0 = \omega\sqrt{\varepsilon_0\mu_0}$  is the free-space wave number.

It can be proven that the continuity of the tangential electromagnetic fields and the ABC are equivalent to [28]:

$$[H_y] = 0, \quad \left[ \frac{1}{\varepsilon_h(z)\varepsilon_t(z)} \frac{dH_y}{dz} \right] = 0, \quad (18)$$

$$\left[ \frac{1}{\varepsilon_t(z)} \frac{d^2 H_y}{dz^2} + \omega^2 \mu_0 \varepsilon_h(z) H_y \right] = 0.$$

In the above the rectangular brackets [...] represent the jump discontinuity of a given quantity at the interface (i.e. the quantity evaluated at the air side subtracted from the quantity evaluated at the rod medium side), and, by definition,  $\varepsilon_h = \varepsilon_0$  and  $\varepsilon_t = 1$  at the free space side. Using these boundary conditions, we readily obtain the following linear system of equations,

$$\begin{pmatrix} -1 & 1 & 1 & 1 & 1 & 0 \\ -\frac{k_z^{(a)}}{\varepsilon_0} & -\frac{k_z^{(1)}}{\varepsilon_h \varepsilon_t} & \frac{k_z^{(1)}}{\varepsilon_h \varepsilon_t} & -\frac{k_z^{(2)}}{\varepsilon_h \varepsilon_t} & \frac{k_z^{(2)}}{\varepsilon_h \varepsilon_t} & 0 \\ -(k_z^{(h)})^2 & \frac{(k_z^{(1)})^2}{\varepsilon_t} & \frac{(k_z^{(1)})^2}{\varepsilon_t} & \frac{(k_z^{(2)})^2}{\varepsilon_t} & \frac{(k_z^{(2)})^2}{\varepsilon_t} & 0 \\ 0 & e^{-jk_z^{(1)}L} & e^{+jk_z^{(1)}L} & e^{-jk_z^{(2)}L} & e^{+jk_z^{(2)}L} & -1 \\ 0 & -\frac{k_z^{(1)}}{\varepsilon_t} e^{-jk_z^{(1)}L} & \frac{k_z^{(1)}}{\varepsilon_t} e^{+jk_z^{(1)}L} & -\frac{k_z^{(2)}}{\varepsilon_t} e^{-jk_z^{(2)}L} & \frac{k_z^{(2)}}{\varepsilon_t} e^{+jk_z^{(2)}L} & \frac{k_z^{(a)}}{\varepsilon_0} \\ 0 & \frac{\varepsilon_h \varepsilon_t}{(k_z^{(1)})^2} e^{-jk_z^{(1)}L} & \frac{\varepsilon_h \varepsilon_t}{(k_z^{(1)})^2} e^{+jk_z^{(1)}L} & \frac{\varepsilon_h \varepsilon_t}{(k_z^{(2)})^2} e^{-jk_z^{(2)}L} & \frac{\varepsilon_h \varepsilon_t}{(k_z^{(2)})^2} e^{+jk_z^{(2)}L} & -(k_z^{(h)})^2 \end{pmatrix} \begin{pmatrix} \rho \\ A_1 \\ A_2 \\ B_1 \\ B_2 \\ T \end{pmatrix} = \begin{pmatrix} 1 \\ -\frac{k_z^{(a)}}{\varepsilon_0} \\ (k_z^{(h)})^2 \\ 0 \\ 0 \\ 0 \end{pmatrix} \quad (19)$$

where we defined  $k_z^{(h)} = -j\sqrt{k_{\parallel}^2 - \varepsilon_h\mu_0\omega^2}$ . In general, the solution of system (19) must be obtained numerically. In the particular case where the rods are embedded in air ( $\varepsilon_h = \varepsilon_0$ ), and within the approximation  $\varepsilon_t = 1$ , the transmission coefficient  $T$  can be written in a compact closed analytical form (an analogous result was obtained in [15] for the case of perfectly conducting rods):

$$T = \frac{1}{1 + \frac{jk_z^{(1)}}{k_z^{(a)}} \tan\left(\frac{k_z^{(1)}L}{2}\right) \frac{(k_z^{(a)})^2 - (k_z^{(2)})^2}{(k_z^{(1)})^2 - (k_z^{(2)})^2} + \frac{jk_z^{(2)}}{k_z^{(a)}} \tan\left(\frac{k_z^{(2)}L}{2}\right) \frac{(k_z^{(a)})^2 - (k_z^{(1)})^2}{(k_z^{(2)})^2 - (k_z^{(1)})^2}}{1 - \frac{jk_z^{(1)}}{k_z^{(a)}} \cot\left(\frac{k_z^{(1)}L}{2}\right) \frac{(k_z^{(a)})^2 - (k_z^{(2)})^2}{(k_z^{(1)})^2 - (k_z^{(2)})^2} - \frac{jk_z^{(2)}}{k_z^{(a)}} \cot\left(\frac{k_z^{(2)}L}{2}\right) \frac{(k_z^{(a)})^2 - (k_z^{(1)})^2}{(k_z^{(2)})^2 - (k_z^{(1)})^2}} \quad (20)$$

In order to validate the proposed ABC and the derived formulas, next we compare the results yielded by our homogenization theory against full wave numerical simulations [29]. We consider that the rods are made of silver, as in section III. The frequency is 30 THz, the lattice constant is 215nm ( $\beta a = 0.2$ ), the radius is  $R = 21.5\text{nm}$  ( $R = 0.1a$ ), and the length of the rods is  $L = 5.93\mu\text{m}$  ( $\beta L = 1.76\pi$ ). As before, the rods are embedded in a host medium with  $\varepsilon_h/\varepsilon_0 = 2.2$ .

In Fig. 5 and Fig. 6 we depict the amplitude and phase, respectively, of the transmission coefficient as a

function of  $k_{\parallel}/\beta$ . The star symbols represent the full wave simulations, whereas the dashed line represents the analytical results. Note that for evanescent waves the transmission coefficient may be larger than unity without violating the conservation of energy. As seen, the agreement is not very satisfactory, particularly for the evanescent spatial harmonics ( $k_{\parallel} > \beta_0$ ). After extensive numerical simulations, we found out that apparently the justification is that the analytical model (3) may slightly underestimate the propagation constant  $k_z^{(1)}$ . This means

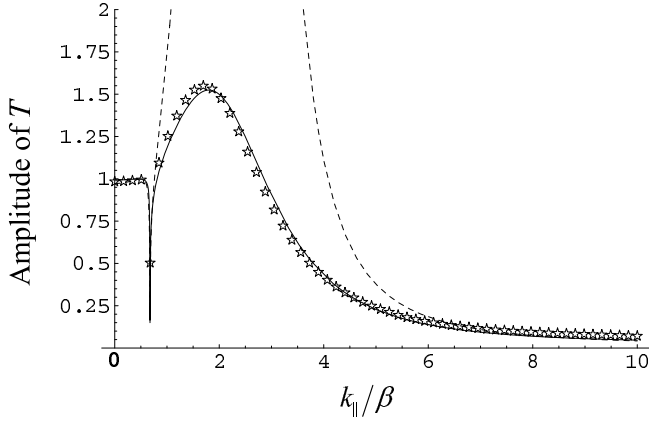


FIG. 5: Amplitude of the transmission coefficient as a function of  $k_{\parallel}/\beta$  for silver rods at 30 THz. The "stars" represent the full wave result, the dashed line represents the analytical result, and the solid line corresponds to the analytical result with corrected  $k_z^{(1)}$ .

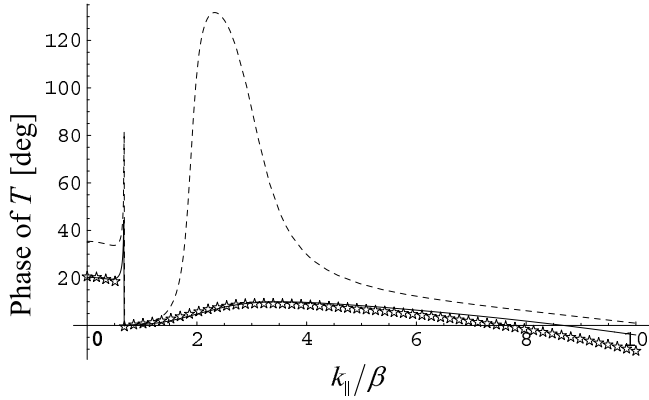


FIG. 6: Phase of the transmission coefficient as a function of  $k_{\parallel}/\beta$  for silver rods at 30 THz. The legend is as in figure 5.

that the propagation velocity along  $z$  is slightly less than the velocity of light in the host medium. This second order effect may be caused by the effect of higher order multipoles. A simple way to obtain more accurate results is to multiply  $k_z^{(1)}$  by a correction factor. The correction factor depends, of course, on the geometry of the crystal and on the permittivity of the rods (for perfectly conducting rods no correction factor is required). For the set of parameters of this example, we verified that the correction factor is 1.04 (around 30 THz). The transmission coefficient calculated with the corrected  $k_z^{(1)}$  corresponds to the solid line in Fig. 5 and Fig. 6. As seen, the agreement becomes very good. Similar results are obtained for the reflection coefficient and other geometries. We stress that the correction factor is independent of  $L$ , and thus the analytical model is very convenient to make parametric studies and understand the electromagnetic response of the rod medium slab.

## V. DIMENSIONING OF THE SLAB THICKNESS

In this section, we will study the imaging properties of the system depicted in Fig. 2, and discuss how the length  $L$  of the rods is chosen. As is well-known, a wave at the front plane,  $z = 0$ , of the imaging system can be decomposed into spatial harmonics. Each Fourier harmonic is associated with a different transverse wave vector  $\mathbf{k}_{\parallel}$ . Because of the superimposition principle, the Fourier harmonics travel independently through rod medium slab. Thus, the transmission coefficient  $T$  can be regarded as a transfer function. For the ideal reconstruction of the image at the output plane  $z = L$ , the amplitude and phase of  $T$  should be ideally independent of  $k_{\parallel}$  (we note here parenthetically that for our system this may be possible only for the spatial harmonics with TM- $z$  polarization; the TE- $z$  Fourier harmonics are not guided by the metallic rods).

In order to make  $T$  independent of  $k_{\parallel}$ , it was suggested in [12] to operate the transmission device under a Fabry-Perot resonance. More specifically, one should choose  $L$  in such a way that:

$$k_z^{(1)}L = n\pi, \quad n = 1, 2, \dots \quad (21)$$

Note that the integer  $n$  determines the thickness of the system. Provided single mode operation can be assumed (i.e. provided the effect of the evanescent TM-mode can be ignored) it is straightforward to prove that the transmission coefficient becomes  $T = \mp 1$ , where the "-" sign is chosen for  $n$  odd, and "+" sign for  $n$  even. The remarkable result [12] is that if  $k_z^{(1)}$  is independent of  $k_{\parallel}$ , the Fabry-Perot condition is fulfilled simultaneously for all the spatial harmonics, and so the imaging system is perfect. In practice, the resolution of the system will be limited by the evanescent TM-mode, and also by the dispersion in the phase velocity of the quasi-TEM mode.

First we analyze the effect of the evanescent mode. For simplicity, we will assume that the rods are embedded in air so that the analytical formula (20) can be used. Taking into account the Fabry-Perot resonance condition (21), and assuming that the evanescent TM-mode is very much attenuated across the slab,  $\text{Im}\{-k_z^{(2)}L\} \gg 1$ , we obtain that:

$$T \approx \mp \frac{1}{1 + \frac{k_z^{(2)}}{k_z^{(a)}} \frac{(k_z^{(a)})^2 - (k_z^{(1)})^2}{(k_z^{(2)})^2 - (k_z^{(1)})^2}} \quad (22)$$

where the "-" and "+" signs are chosen as before. Since  $k_z^{(a)}$  and  $k_z^{(1,2)}$  are in general functions of  $k_{\parallel}$ , the above expression also is, and the imaging is not perfect, even in the case of perfectly conducting rods where  $k_z^{(1)}$  is exactly dispersionless [15]. When the attenuation constant of the evanescent mode is very large,  $|k_z^{(2)}| \gg |k_z^{(a)}|$  and  $|k_z^{(2)}| \gg |k_z^{(1)}|$ , equation (22) yields  $T \approx \mp 1$ , i.e. the result that we got when assuming single mode operation.

Let us discuss now the effect of non-flat isofrequency contours for the quasi-TEM mode, i.e. the consequences of  $k_z^{(1)}$  being a function of  $k_{\parallel}$ . This non-ideal behavior means that there is no collective Fabry-Perot resonance: the electrical length corresponding to the resonance becomes a function of  $k_{\parallel}$ . Thus, even if the effect of the evanescent TM-mode could be neglected, the imaging would not be perfect. Indeed, from section II we know that  $k_z^{(1)}$  has the following bounds:

$$k_0^{(1)} \leq k_z^{(1)}(k_{\parallel}) \leq k_{\infty}^{(1)} \quad (23)$$

Hence, to recover a certain spectral component of the image at the output plane,  $L$  must be chosen such that it satisfies (21) for the pertinent  $k_{\parallel}$ , and consequently the optimum  $L$  becomes a function of  $k_{\parallel}$ :

$$L_{\infty} \leq L \leq L_0 \quad (24)$$

In above,  $L_{0,\infty} = \text{Re} \left\{ n\pi/k_{0,\infty}^{(1)} \right\}$ . Note that  $L_0$  can be written as  $L_0 = \frac{n\lambda_h}{2\varepsilon_t}$ , where  $\lambda_h$  is the wavelength in the host material.

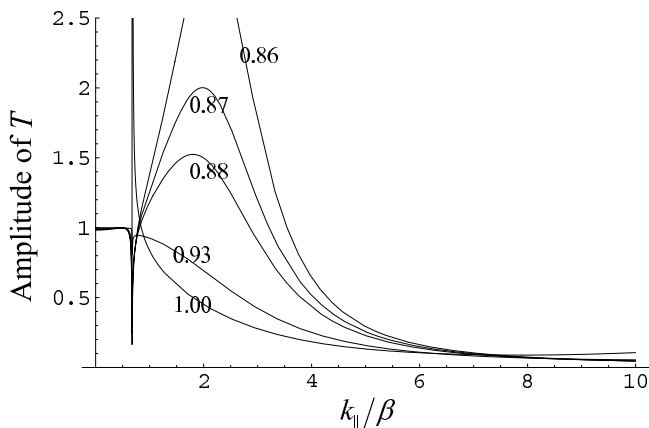


FIG. 7: Amplitude of the transmission coefficient as a function of  $k_{\parallel}/\beta$  for silver rods at 30 THz. The length of the rods is  $L = q\lambda_h$ , where  $\lambda_h = 6.74\mu\text{m}$  and  $q = 1.00, 0.93, 0.88, 0.87, 0.86$  (each value of  $q$  is associated with a different curve).

In practice, how should one choose  $L$ ? If we want to recuperate only the propagating waves, the choice  $L = L_0$  is adequate. However, in general, the condition  $L = L_0$  is not appropriate for the evanescent harmonics with  $k_{\parallel} > \beta_0$ . For these modes the Fabry-Perot condition is fulfilled for some length  $L(k_{\parallel}) < L_0$ . Thus, in order that near-field imaging is possible, we may have to make a trade-off. More specifically, we may have to allow some phase and/or amplitude distortion for the propagating waves, in order to improve transmission of the evanescent waves. Thus, the length  $L$  will be chosen in the interval defined by (24).

To illustrate the discussion let us consider an example. Again, we consider silver rods at 30 THz, with the same

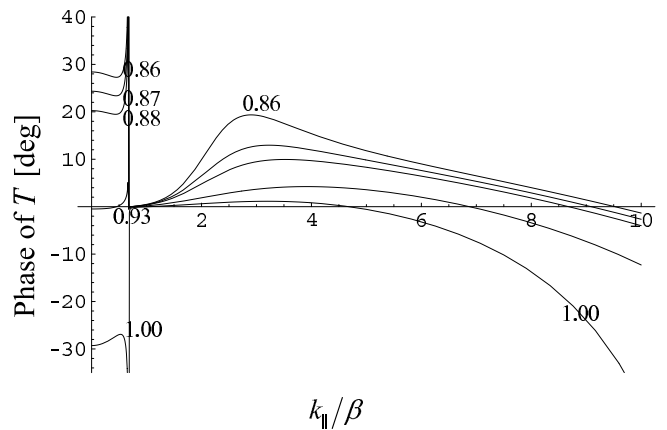


FIG. 8: Phase of the transmission coefficient as a function of  $k_{\parallel}/\beta$  for silver rods at 30 THz. The length of the rods is  $L = q\lambda_h$ , where  $\lambda_h = 6.74\mu\text{m}$  and  $q = 1.00, 0.93, 0.88, 0.87, 0.86$ .

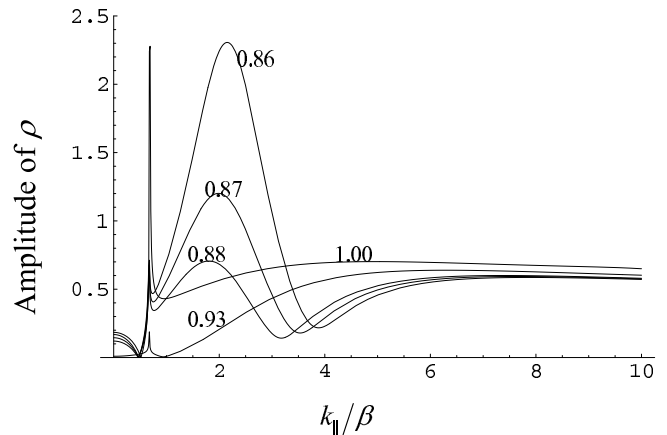


FIG. 9: Amplitude of the reflection coefficient as a function of  $k_{\parallel}/\beta$  for silver rods at 30 THz. The length of the rods is  $L = q\lambda_h$ , where  $\lambda_h = 6.74\mu\text{m}$  and  $q = 1.00, 0.93, 0.88, 0.87, 0.86$ .

lattice constant, host medium, and radius as in the previous section. In Fig. 7 and Fig. 8 the amplitude and phase of the transmission coefficient are plotted for different values of  $L$ . We used the analytical model (20) to plot the curves, taking also into account the correction factor 1.04 to better predict  $k_z^{(1)}$ , as discussed in the previous section. It is seen that when the thickness of the rods is close to  $0.93\lambda_h$  (which corresponds to the  $n = 2$  Fabry-Perot resonance with  $L = L_0$ , using the correction factor 1.04), the transmission coefficient is  $T \approx 1$  for the propagating waves. However, the amplitude response of the evanescent waves is relatively poor. As discussed before, the response of the evanescent spectrum can be improved by decreasing  $L$ . It is seen that when this is done the phase of  $T$  for the propagating waves becomes progressively more distant from zero, even though it remains relatively flat. However, the amplitude response of the evanescent spectrum is significantly improved, and for  $L = 0.88\lambda_h = 5.93\mu\text{m}$ , near field imaging seems possible



roughly for  $k_{\parallel}/\beta < 3.5$  with relatively small phase and amplitude distortion. Note, that if  $L$  is greater than  $L_0$  (curve with  $L = 1.00\lambda_h$ ) then the transmission characteristic has a pole very close to  $k_{\parallel}/\beta \approx 1$ . This indicates that for this set of parameters a surface wave is supported by the rod medium slab. This regime must be avoided since the excitation of surface waves and the selective amplification of very specific spatial harmonics leads to destruction of subwavelength imaging [15].

Another important aspect is to avoid interference between the reflected wave and the source. To this end, we need to ensure that the reflection coefficient amplitude remains relatively small in the frequency band of interest. In Fig. 9 it is seen that reflection level is very high for  $L \leq 0.87\lambda_h$ , and so the length of the rods must definitely be chosen larger than  $0.87\lambda_h$ .

To conclude this section, we study the bandwidth of the proposed transmission device. In Fig. 10 the transmission characteristic is depicted for different frequencies assuming that the length of the rods is  $L = 5.93\mu\text{m}$  (corresponds to  $q = 0.88$  at 30THz). It is seen that the effect of changing frequency for a fixed  $L$  is qualitatively similar to the effect of changing  $L$  for a fixed frequency (Fig. 7).

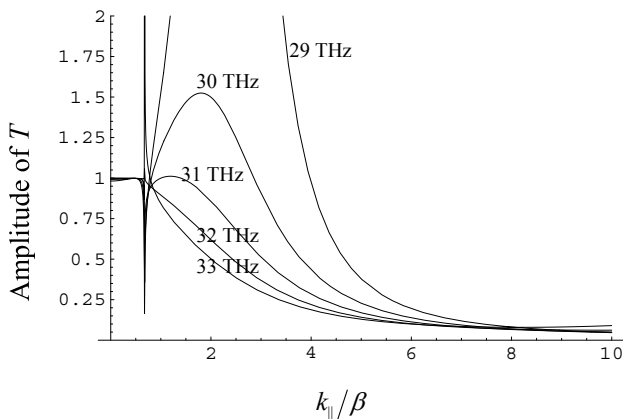


FIG. 10: Amplitude of the transmission coefficient as a function of  $k_{\parallel}/\beta$  for silver rods at different frequencies. The length of the rods is  $L = 5.93\mu\text{m}$ .

## VI. NEAR-FIELD IMAGING AT INFRARED FREQUENCIES

Next, we illustrate the possibilities and potentials of the proposed subwavelength imaging mechanism. To this end, we simulated the performance of a rod medium slab that consists of an array of  $89 \times 69$  silver nanorods (see Fig. 11) using CST Microwave Studio full-wave electromagnetic simulator [29]. The nanorods are embedded in Halcoenide glass ( $\epsilon_h = 2.2\epsilon_0$ ) with total dimensions of  $19.35 \times 15.05 \times 5.93\mu\text{m}$ . The lattice constant is  $a = 215\text{nm}$ , the radius of the rods is  $R = 21.5\text{nm}$ , and the

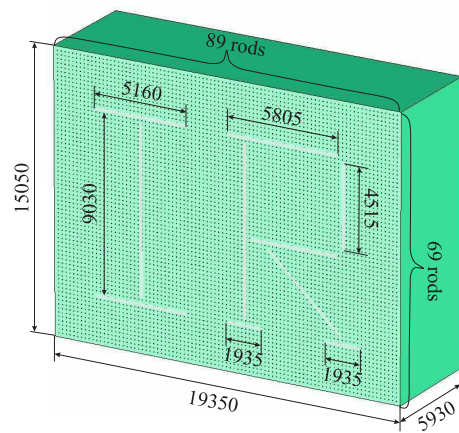


FIG. 11: Geometry of finite-sized slab of rod medium used in full-wave simulation. The critical parameters are given in nm.

length of the rods is  $L = 5.93\mu\text{m}$ , consistently with the simulations presented in the previous sections. Namely, at 30THz the dispersion contours of the electromagnetic modes are presented in Fig. 3 and Fig. 4 (curve with  $R = 0.1a$ ) and the transmission coefficient is shown in Fig. 10 for different frequencies. We stress that in all the simulations presented in this paper the effect of realistic losses in silver is taken into account.

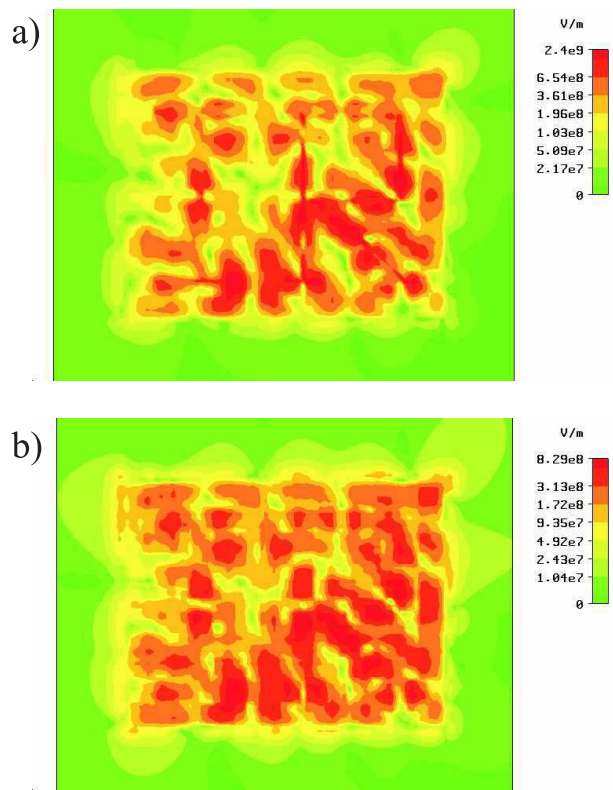


FIG. 12: Distributions of  $|E_z|$  at 29THz: a) at the source plane, at distance  $a/2$  from the source and at the distance  $a$  from the front interface, and b) at the image plane, at distance  $a/2$  from the back interface.

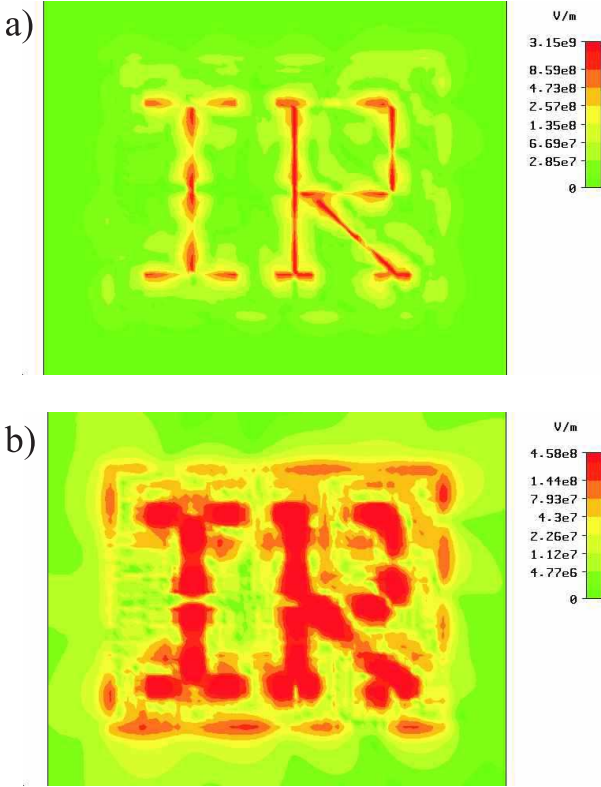


FIG. 13: Distributions of  $|E_z|$  at 30THz: a) at the source plane, and b) at the image plane.

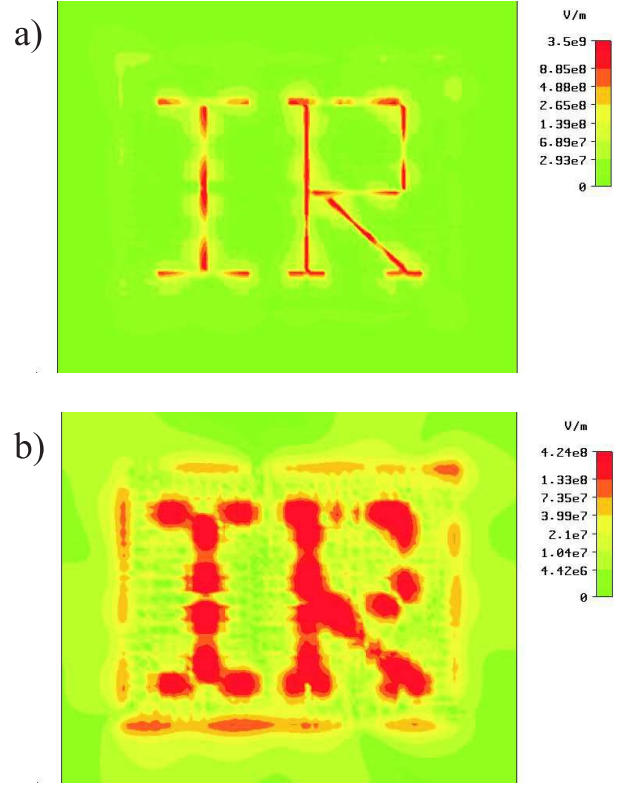


FIG. 14: Distributions of  $|E_z|$  at 31THz: a) at the source plane, and b) at the image plane.

In our numerical model the source consists of a set of perfectly conducting wire dipoles driven by 1A currents in their centers and arranged in the form of letters "IR", see Fig. 11. The source is placed at the distance  $a/2 = 107.5\text{nm}$  from the front interface. The "IR"-shaped dipole source radiates both TE- $z$  and TM- $z$  waves. As discussed before, the rod medium slab is able to guide only the TM- $z$  spatial harmonics. Thus, in order to evaluate the waveguiding properties of the rod medium slab we numerically calculated the  $z$ -component of the electric field at the front (input) plane and at the back (output) plane. More specifically, the field is calculated at the distance  $a/2$  from the source and back interface, respectively. Note, that the  $z$ -component of electrical field includes only the contribution of TM- $z$  waves since  $E_z = 0$  for the TE- $z$  waves.

In Fig. 12  $|E_z|$  is depicted at 29THz at the input and output planes, respectively. It is clear that the imaging properties are very poor, and that the letters "IR" are hardly perceptible in the image, even at the front interface. As discussed in section V, the reason for this phenomenon is related with the strong reflections from the rod medium slab due to the resonant excitation of surface waves.

At higher frequencies, for example at 30THz and 31THz, see Fig. 13 and Fig. 14, the imaging properties are excellent. In this frequency range the surface wave mode cannot be excited and so there is little interaction

between the transmission device and the source. Due to this reason the "IR" shaped letters are sharply defined in the near-field distribution at the source plane (Fig. 13 and Fig. 14). Also, consistently with our theoretical model, the rod transmission device is able to canalize the image from the front interface to the back interface with subwavelength resolution. The best imaging occurs at 31THz. We can estimate the resolution (minimum distance that makes two point sources resolved) of the transmission device as explained next. From Fig. 10 it is seen that at 30THz,  $T > 0.7$  (half-power criterion) for  $k_{\parallel} < 3.43\beta$ , or equivalently for  $k_{\parallel} < 5.1\beta_0$ . Thus, the resolution of the transmission device is about 5.1 times better than that of free-space, i.e. the resolution is around  $\lambda_0/(2 \times 5.1) = \lambda_0/10.2$ . This rough criterion is consistent with the resolution estimated directly from the image. It can be checked that the thickness of the stem of letter "I" at the back interface is approximately  $5a \approx \lambda_0/9.3$ . This implies that the resolution is around  $\lambda_0/9.3$ .

For frequencies larger than 31THz the imaging properties are slightly deteriorated, as it could be anticipated from Fig. 10, but subwavelength resolution is still observed. This is illustrated in Fig. 15 and Fig. 16 for 33THz and 36THz, respectively. At 36THz the image is not so clear as at lower frequencies, and thus we can treat 35 THz as the upper bound of the frequency band where imaging with good sub-wavelength resolution is observed (the lower bound is roughly at 30 THz). It is

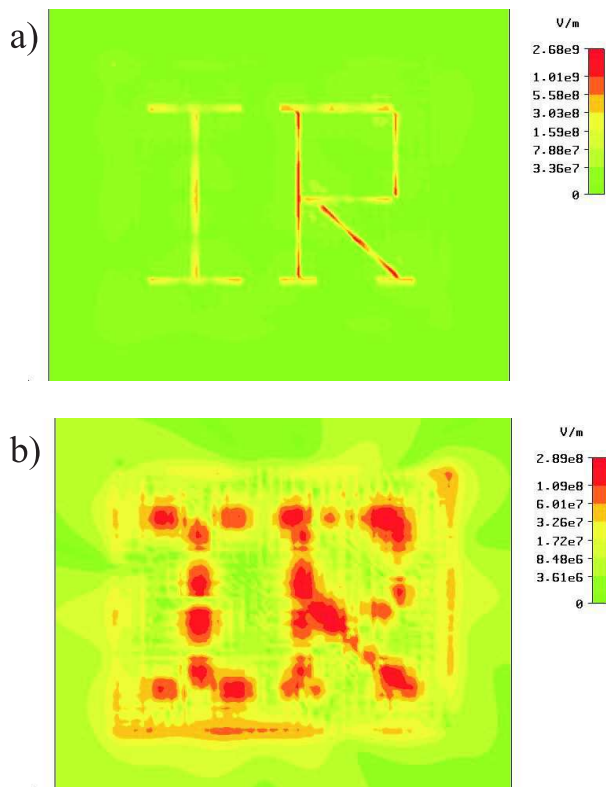


FIG. 15: Distributions of  $|E_z|$  at 33THz: a) at the source plane, and b) at the image plane.

thus clear that the bandwidth of the proposed waveguiding mechanism is very good: around 15%, unlike in other configurations proposed in the literature (e.g. [1]). Indeed, our conceptual approach is very different from other works. In our structure we are not directly exploring a resonance of the artificial material, but instead we are only exploiting the fact that metallic rods support a quasi-TEM dispersionless mode, which is by itself a very broadband phenomenon.

For frequencies below 30THz the resolution and bandwidth of a properly scaled transmission device can always be improved [14, 15]. This is a direct consequence of silver becoming a better electrical conductor. It is also worth mentioning that it is possible to get even better results at 30THz and higher frequencies by using aluminium (Al) rods (aluminium has a larger plasma frequency than silver), or alternatively by using rods made of a material with an absorption peak at the frequency band of interest. However, it is questionable if moving to higher frequencies is meaningful because there are practical limits in the realization of the nanorods.

## VII. CONCLUSION

In this work, we assessed the possibility of near-field sub-wavelength imaging at infrared frequencies using array of thin silver rods. Using the homogenization model

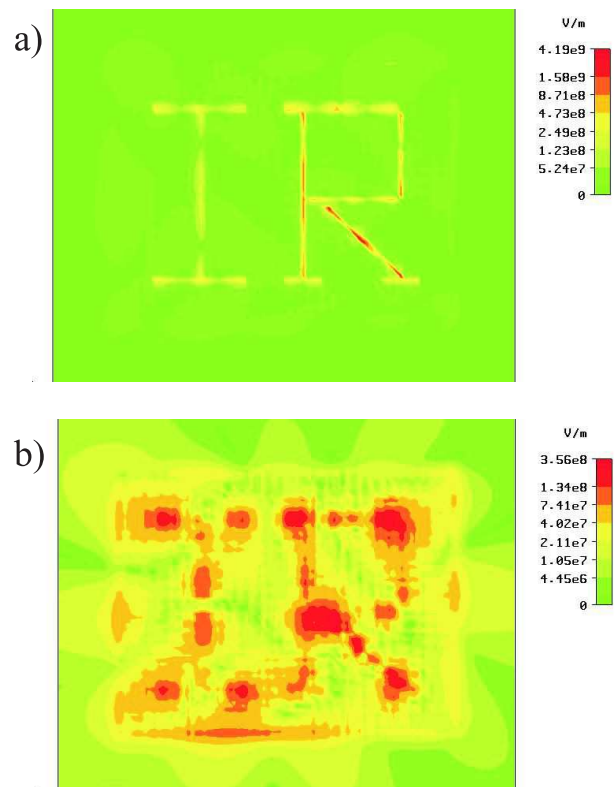


FIG. 16: Distributions of  $|E_z|$  at 36THz: a) at the source plane, and b) at the image plane.

proposed in [17], we studied the dimensioning of the rods and of the array. It was discussed that the plasmonic rod medium should be operated in the regime where it supports a quasi-TEM mode. It was seen that subwavelength imaging is possible only if the isofrequency contour of the quasi-TEM mode is nearly flat, and, additionally, if the second TM-mode is strongly attenuated. In order to fulfill these conditions and guarantee good matching with free-space, it is necessary that the radius of the rods is larger than the skin-depth of the metal, that the lattice constant is much smaller than the wavelength, and that  $R/a$  is small. In general it may not be possible to attain all the conditions simultaneously, and so a compromise may be necessary. It was demonstrated that an additional boundary condition is necessary to calculate the transmission characteristic of the rod medium slab using homogenization methods. It was proved that the proposed analytical formulation accurately characterizes the interaction of waves with the plasmonic rods, and allows to qualitatively understand the physics of the pertinent phenomena. To study the potentials and possibilities of the proposed subwavelength imaging mechanism, we numerically simulated the performance of an array of plasmonic rods excited by an "IR" shaped near field source. Consistently with our theoretical study, subwavelength imaging with resolution  $\lambda_0/10$  and 15% bandwidth was demonstrated.

- 
- [1] J. Pendry, Phys. Rev. Lett. **85**, 3966 (2000).
- [2] N. Garcia and M. Nieto-Vesperinas, Phys. Rev. Lett. **88**, 207403 (2002).
- [3] D. R. Smith, D. Schurig, M. Rosebluth, S. Schultz, S. Anantha-Ramakrishna, and J. B. Pendry, Appl. Phys. Lett. **82**, 1506 (2003).
- [4] V. A. Podolskiy and E. E. Narimanov, Opt. Lett. **30**, 75 (2005).
- [5] C. Luo, S. G. Johnson, J. D. Joannopoulos, and J. Pendry, Phys. Rev. B **65**, 201104 (2002).
- [6] C. Luo, S. G. Johnson, J. D. Joannopoulos, and J. Pendry, Phys. Rev. B **68**, 045115 (2003).
- [7] M. J. Freire and R. Marques, Appl. Phys. Lett. **86**, 182505 (2005).
- [8] Z.-Y. Li and L.-L. Lin, Phys. Rev. B **68**, 245110 (2003).
- [9] H.-T. Chien, H.-T. Tang, C.-H. Kuo, C.-C. Chen, and Z. Ye, Phys. Rev. B **70**, 113101 (2004).
- [10] C.-H. Kuo and Z. Ye, Phys. Rev. E **70**, 056608 (2004).
- [11] X. Zhang, Phys. Rev. B **70**, 205102 (2004).
- [12] P. A. Belov, C. R. Simovski, and P. Ikonen, Phys. Rev. B **71**, 193105 (2005).
- [13] P. Ikonen, P. Belov, C. Simovski, and S. Maslovski, Phys. Rev. B **73**, 073102 (2006).
- [14] P. A. Belov, Y. Hao, and S. Sudhakaran, Phys. Rev. B **73**, 033108 (2006).
- [15] P. A. Belov and M. Silveirinha, Phys. Rev. E **73**, 056607 (2006).
- [16] A. Ono, J. ichi Kato, and S. Kawata, Phys. Rev. Lett. **95**, 267407 (2005).
- [17] M. Silveirinha, Phys. Rev. E **73**, 046612 (2006).
- [18] D. E. Mittleman, *Sensing with Terahertz Radiation* (Springer, Heidelberg, 2002).
- [19] P. Belov, R. Marques, S. Maslovski, I. Nefedov, M. Silveirinha, C. Simovski, and S. Tretyakov, Phys. Rev. B **67**, 113103 (2003).
- [20] M. A. Ordal, R. J. Bell, R. W. A. Jr, L. L. Long, and M. R. Querry, Applied Optics **24**, 4493 (1985).
- [21] M. A. Ordal, L. L. Long, R. J. Bell, S. E. Bell, R. R. Bell, R. W. A. Jr., and C. A. Ward, Applied Optics **22**, 1099 (1983).
- [22] P. B. Johnson and R. W. Christy, Phys. Rev B **6**, 4370 (1972).
- [23] I. El-Kady, M. M. Sigalas, R. Biswas, K. M. Ho, and C. M. Soukoulis, Phys. Rev B **62**, 15299 (2000).
- [24] K. Wang and D. M. Mittleman, Nature (London) **432**, 376 (2004).
- [25] Q. Cao and J. Jahns, Optics Express **13**, 511 (2005).
- [26] J. Takahara, S. Yamagishi, H. Taki, A. Morimoto, and T. Kobayashi, Optics Letters **22**, 475 (1997).
- [27] V. Agranovich and V. Ginzburg, *Spatial dispersion in crystal optics and the theory of excitons* (Wiley- Interscience, NY, 1966).
- [28] M. Silveirinha, IEEE Trans. Antennas. Propagat. **54**, 1766 (2006).
- [29] (CST Microwave StudioTM 5.0, CST of America, Inc., www.cst.com).